Modeling thermoelectric properties of monolayer and bilayer WS$_2$ by including intravalley and intervalley scattering mechanisms

Raveena Gupta

Institute of Nano Science and Technology, Sector-81, Knowledge City, Sahibzada Ajit Singh Nagar, Punjab, Pin 140306, India
and Centre for Nanoscience and Nanotechnology, Panjab University, Sector-25, Chandigarh 160036, India

Chandan Bera ◉*

Institute of Nano Science and Technology, Sector-81, Knowledge City, Sahibzada Ajit Singh Nagar, Punjab, Pin 140306, India

Herein, we investigate the impact of all electron and phonon scattering mechanisms on the electrical and thermal transport properties of the monolayer and bilayer transition-metal dichalcogenide WS$_2$. We used the Boltzmann transport equation under the relaxation-time approximation to calculate both the electron and phonon transport properties. Due to multiple valleys near the Fermi energy level, intervalley scattering is seen as the prominent scattering mechanism that critically impacts the electrical transport properties in both of these materials. The power factor reduces by 93% and 83% for monolayer and bilayer WS$_2$, respectively, due to intervalley scattering leading to almost equal values for both materials at room temperature. Earlier theoretical reports on monolayer WS$_2$ overestimated the experimentally observed lattice thermal conductivity values. Experimental observations suggest that when monolayer and bilayer WS$_2$ is formed, defects might be present in these systems, affecting phonon transport. We found that defect scattering significantly contributes to phonon scattering when the relative sulfur vacancy concentration exceeds 0.01 for both monolayer and bilayer WS$_2$, resulting in a remarkable 99% agreement with experimental values. A high $ZT \sim 3$ is attained for monolayer WS$_2$ as compared to $ZT \sim 2$ for bilayer WS$_2$ at 800 K because of the higher thermal conductivity of the bilayer due to elevated group velocities of its optical-phonon modes. This work presents a deep insight into the scattering mechanisms controlling the thermoelectric performance of monolayer and bilayer WS$_2$.

I. INTRODUCTION

Layered transition-metal dichalcogenides (TMDs) are receiving tremendous attention as their promising properties lead to their vast application in electronics, optoelectronics, and thermoelectrics (TE) [1–3]. One of the foremost reasons TMDs such as MoS$_2$ and WS$_2$ are being studied theoretically and experimentally [4–9] is because of the qualitatively different properties, such as indirect- to direct-band-gap transition and increments of electron-hole correlations, exhibited by them as we go from bulk to a few layers to monolayers [10,11]. Recently, electron transport properties of monolayer WS$_2$ were investigated theoretically by Wickramaratne *et al.* [7] using a constant relaxation-time approach. Though the effect of intravalley electron-phonon scattering on electrical transport properties has been studied extensively [12,13], the intervalley scattering mechanism has not been investigated thoroughly. As WS$_2$ monolayer and bilayer possess multiple valleys near the Fermi level within a narrow energy range, they can induce strong intervalley scattering. Both acoustic and optical phonons can cause electron transitions between states in different conduction-band valleys of these materials. These transitions can improve thermoelectric performance by

elevating the Seebeck coefficient [14]. Hence, it is important to understand how this intervalley scattering and number of valleys tunes the electrical properties in these chalcogenides.

Phonon transport properties of monolayer WS$_2$, on the other hand, were theoretically calculated by Zulfiqar *et al.* [15] using SHENGBTE while they were experimentally investigated by Peimyoo *et al.* [16]. However, there is a 72% difference between thermal conductivity values predicted by theory and experiment. Electron-phonon scattering for phonon transport in traditional semiconductors is neglected due to low carrier concentrations, which leads to weak phonon scatterings from carriers. Only recently, a report by Liu *et al.* [17] studied the effect of electron-phonon interaction on the lattice thermal conductivity of single-layered MoS$_2$ under *p*-type and *n*-type doping. A significant reduction in the lattice thermal conductivity—by 39% at 300 K—was seen at a carrier concentration of 6.5×10^{13} cm^{-2} upon including the effect of these interactions. Due to the narrow band gap of monolayer and bilayer WS$_2$, they possess high carrier concentration, so the effect of electron-phonon scattering in phonon transport should be investigated.

WS$_2$ is one of the emerging materials with the potential to be used in both thermoelectric and optoelectronic devices. Moreover, WS$_2$ has a high intrinsic carrier concentration in the 10^{13} cm^{-2} regime. Hence, in this work, we investigate the effect of intravalley electron-phonon interaction as well

*chandan@inst.ac.in

as intervalley scattering on the electrical transport properties of monolayer and bilayer WS$_2$ in the Boltzmann transport equation framework using a full *ab initio* and a parametrized relaxation-time approach to calculate the transport properties. The effect of defect-phonon interaction is also studied on the thermal transport properties of these materials. Intervalley scattering is seen to play an essential role in tuning electrical transport properties. A high figure of merit ($ZT > 1$), which determines the efficiency of the thermoelectric material, is also predicted for both monolayer and bilayer WS$_2$ at temperatures greater than 500 K.

II. THEORETICAL METHODS

The electronic structure calculations of WS$_2$ monolayer and bilayer are performed using the plane-wave basis projector augmented wave (PAW) [18] method in the framework of density functional theory (DFT) using the Vienna Ab initio Simulation Package (VASP) [19]. The electronic band structure of monolayer and bilayer WS$_2$ is calculated by including the spin-orbit coupling effect, using the Perdew-Burke-Ernzerhof (PBE) [20] exchange-correlation functional within the generalized gradient approximation (GGA). The plane-wave cutoff is set at 500 eV for both materials. The structures are relaxed using a 4×4×1 Monkhorst-Pack grid for integrations over the Brillouin zone (BZ). For the band energies and total energy, a tolerance of 1×10^{-8} eV is set until the absolute value of all elements of the force is lower than 0.01 eVÅ^{-1}.

The electrical transport properties for monolayer and bilayer WS$_2$ are calculated in the Boltzmann transport equation (BTE) framework within the relaxation-time approximation (RTA) using BOLTZTRAP2 [21] and also using the PERTURBO package [22]. In BOLTZTRAP2, under the RTA, the generalized transport coefficients are calculated from the transport distribution function given by Ref. [21],

$$f(E, T) = \int \mathbf{v_k} \otimes \mathbf{v_k} \tau_\mathbf{k} \delta(E - E_\mathbf{k}) \frac{dk}{8\pi^3}. \tag{1}$$

In the above equation, $\mathbf{v_k}$ is the component of the group velocity of each carrier in the transport direction, $E_\mathbf{k}$ is the energy of that electronic state, and $\tau_\mathbf{k}$ is its total relaxation time, which is calculated using Matthiessen's rule, i.e., $\tau^{-1} = \sum_i \tau_i^{-1}$, where i runs over all scattering mechanisms.

The electrical conductivity (σ), Seebeck coefficient (S), and electronic thermal conductivity (κ_e) are expressed in terms of moments of generalized transport coefficients (ζ) as given in Ref. [21]. The transport coefficients are defined as [21]

$$\sigma = \zeta^{(0)}, \tag{2}$$

$$S = \frac{1}{eT} \frac{\zeta^{(1)}}{\zeta^{(0)}}, \tag{3}$$

$$\kappa_{el} = \frac{1}{e^2 T} \left[\frac{\zeta^{(1)2}}{\zeta^{(0)}} - \zeta^{(2)} \right]. \tag{4}$$

The transport of electrons in WS$_2$ is limited by intravalley and intervalley electron-phonon scattering mechanisms. The intravalley electron–acoustic-phonon scattering is captured

using band deformation theory, according to the formula [13]

$$\frac{1}{\tau_{e\text{-ph}_{ac}}} = \frac{k_B T_L \pi N(\epsilon) E_D^2}{u_s^2 \rho \hbar}, \tag{5}$$

where k_B is the Boltzmann constant, T_L the lattice temperature, ρ is the density of the medium, u_s is the speed of sound (monolayer, 2421 ms^{-1}; bilayer, 2918 ms^{-1}) in the medium, and E_D is the deformation potential [23,24]. The value is found to be -11.58 eV for CBM and -5.61 eV for VBM for bilayer WS$_2$ and -10.08 eV for CBM and -4.61 eV for VBM for monolayer WS$_2$. These values are in good agreement with the values reported by Rawat *et al.* [25].

Like the electron scattering by acoustic phonons, the scattering due to optical phonons can be modeled by using the optical deformation potential (D_{op}) as [26,27]

$$\frac{1}{\tau_{e-\text{ph}_{op-abs/em}}} = \frac{D_{op}^2 (2m_e)^{3/2}}{4\pi \hbar^3 \rho \omega_q} \left[\left(N_q + \frac{1}{2} \mp \frac{1}{2} \right) \sqrt{E_k \pm \hbar \omega_q} \right]. \tag{6}$$

In the above equation, ρ is the mass density, E_k is the electron energy, ω_q is the optical phonon frequency, and m_e is the electron mass. The $\mp$ sign in the N_q part represents phonon absorption and emission, respectively, and N_q is the phonon occupation number following the Bose-Einstein statistics,

$$N_q = \frac{1}{e^{\frac{\hbar \omega_q}{k_B T}} - 1}. \tag{7}$$

For emission process, the electron energy has to be greater than the phonon energy. The value of the optical deformation potential is taken from an earlier report [26,27].

For a comparison of electronic properties based on RTA with full *ab initio* scattering rates, DFT and DFPT (density functional perturbation theory) calculations are performed using QUANTUM ESPRESSO [28], followed by Wannier function interpolation with WANNIER90 [29,30] and further calculations with PERTURBO [22]. The same PBE functional as used with VASP [20] along with a k-point mesh of 20×20×1 is used. The energy cutoff is set at 80 Ry in the expansion of the wave functions, and the energy convergence criterion is taken as 1×10^{-10} Ry. A regular dense 80×80×1 k-point grid is used for the interpolation step. In PERTURBO, the BTE is either solved iteratively or by using RTA. In this work, for comparison with model results, the RTA method is used, which is computed as in Ref. [22].

As the material under consideration has multiple valleys, the influence of intervalley scattering is also considered. The intervalley scattering can be formally treated in the same way as intravalley scattering by optical phonons [31,32]. This scattering is given by

$$\frac{1}{\tau_{iv}} = \sum_j \frac{m_j^{3/2} D_{ij}^2}{\sqrt{2}\pi \rho \hbar^3 \omega_{ij}} [N_{ij}(E - \Delta E_{ij} + \hbar \omega_{ij})^{1/2} + (N_{ij} + 1)$$
$$\times (E - \Delta E_{ij} + \hbar \omega_{ij})^{1/2} \Theta(E - \Delta E_{ij} + \hbar \omega_0)]. \tag{8}$$

In the above equation, the summation is over the valleys where scattering occurs. $N_{ij} = \frac{1}{e^{\frac{\hbar \omega_{ij}}{k_B T}} - 1}$ is the phonon occupation number, D_{ij} is the valley deformation potential (for WS$_2$

the values are considered from a report by Jin *et al.* [27]), m_j is the effective mass of an electron at the jth valley, ρ is the mass density, E is the electron energy, ΔE_{ij} is the energy difference between two valleys, ω_0 is the phonon energy at a particular valley, and ω_{ij} is the phonon energy between two valleys. Θ is the Heaviside function, which determines if the transition is possible. The intervalley scattering rate has a $T^{-3/2}$ mobility dependence.

For lattice thermal conductivity calculation of monolayer and bilayer WS_2, the force constants are first extracted using a real-space approach as implemented in the PHONOPY [33] package. $4\times4\times1$ supercells and displacements with an amplitude of 0.01 Å are used for calculating forces with VASP to obtain interatomic force constants. The lattice thermal conductivity in the RTA is given by [34]

$$\kappa_l = \sum_b \int \frac{d^3\mathbf{q}}{8\pi^3} v_{b,\mathbf{q}}^2 \tau_{b,\mathbf{q}} C_{b,\mathbf{q}}, \tag{9}$$

where the sum is over all phonon bands b, the integral is over all the Brillouin zone, $v_{b,\mathbf{q}}$ is the group velocity of a given phonon mode along the chosen direction, $\tau_{b,\mathbf{q}}$ is the mode relaxation time, and $C_{b,\mathbf{q}}$ is the mode heat capacity, dependent on the mode frequency $\omega_{b,\mathbf{q}}$ and temperature. $v_{b,\mathbf{q}}$ and $C_{b,\mathbf{q}}$ are directly calculated from the phonon band structure. First, the umklapp scattering process is used to approximate the relaxation time needed for thermal transport properties, and it is given as [34,35]

$$\frac{1}{\tau_U} = p\omega^2 \frac{T}{\tilde{\theta}_D} e^{-\frac{\tilde{\theta}_D}{3T}}, \tag{10}$$

where p is an adjustable parameter given by Ref. [12]. The Debye temperature is obtained from the second moment of the entire phonon spectrum as [34,36]

$$\tilde{\theta}_D = n^{-1/3} \sqrt{\frac{5\hbar^2}{3k_B^2} \frac{\int_0^\infty \omega^2 g(\omega)d\omega}{\int_0^\infty g(\omega)d\omega}}. \tag{11}$$

In the above equation, n is the number of atoms per unit cell. The mode averaged-squared Grüneisen parameter ($\tilde{\gamma}^2$) is given by [37]

$$\tilde{\gamma}^2 = \frac{\sum_i \int \frac{dq}{8\pi^3} \gamma_{iq}^2 C_{iq}}{\sum_i \int \frac{dq}{8\pi^3} C_{iq}}. \tag{12}$$

The volume derivatives needed to obtain $\tilde{\gamma}^2$ for the RTA calculation are also derived from the finite-difference method based on computations for a defined range of volumes.

Experimental observations suggest that the ratios of W to S may not always maintain their 1:2 ratio when monolayer or bilayer WS_2 is formed [38]. Therefore, the defect scattering rate is also included and is given by [39]

$$\frac{1}{\tau_D} = c\Gamma_M \frac{V}{4\pi n s^3} \omega^4, \tag{13}$$

where c ($= 0.03$) is the relative concentration of vacancies or defects, V/n is the volume per atom, s is the speed of sound, and Γ_M is the mass difference scattering strength parameter given by [39]

$$\Gamma_M = \left(\frac{M_V}{M} + 2\right)^2. \tag{14}$$

In the above equation, M_V is the mass of the missing atom.

To compare the umklapp scattering rates in monolayer WS_2, we also computed the lattice thermal conductivity using both full *ab initio* and RTA methods as implemented in the ALMABTE [40] software package. To obtain the lattice thermal conductivity using ALMABTE, we required sets of second- and third-order force constants. The second-order force constants obtained by PHONOPY were postprocessed to preserve the rotational symmetry of free space [41]. To obtain the third-order force constants, we performed supercell calculations with a supercell size of $4\times4\times1$, considering interactions up to third-nearest neighbors using the thirdorder.py script [42]. These force constants were then used to calculate the allowed three-phonon scattering processes. All DFT calculations for supercells were Γ-only and used the same set of parameters as the initial relaxation. To solve the phonon BTE and compute the thermal conductivity, phonon properties were sampled with ALMABTE on a dense $30\times30\times1$ grid, which was obtained through proper convergence study for the WS_2 structure.

It is important to note that for the transport properties calculations for both electrons and phonons, the coefficients are resized by a factor of c/h, where c (23 Å for monolayer WS_2 and 43 Å for bilayer WS_2) is the total distance including vacuum along the z-direction, and h (8.01 Å for monolayer WS_2 and 18.2 Å for bilayer WS_2) is the thickness of the layered systems. Finally, using both the electrical and thermal transport coefficients, the figure of merit is calculated as

$$ZT = \frac{S^2\sigma T}{\kappa_e + \kappa_l}. \tag{15}$$

III. RESULTS AND DISCUSSION

Monolayer and bilayer WS_2 belong to the hexagonal crystal family. Their crystal structures are illustrated in the first column of Figs. 1(a) and 1(b), respectively. Single-layer WS_2 belongs to space group $P\bar{6}m2$. The lattice constant is calculated to be 3.18 Å, which is in $\sim$99% agreement with the previous report [43]. WS_2 bilayer is constructed according to AA' stacking where one layer is flipped by 180°. The calculations are done on AA' stacking as it is one of the most stable configurations as reported by Li *et al.* [44]. The interlayer distance is minimal in this type of stacking conformation, indicating a very strong interaction. Bilayer WS_2 belongs to the trigonal $P\bar{3}m1$ space group.

The calculated electronic band structure of 2H-WS_2 monolayer with the spin-orbit coupling (SOC) effect is shown in the second column of Fig. 1(a). WS_2 monolayer has a direct band gap of 1.61 eV. The inclusion of SOC splits the valence bands at high symmetry point K. As a result, one of the degenerate valence bands shifts upwards, reducing the band gap. Both the valence-band maxima (VBM) and the conduction-band minima (CBM) are dominated by the heavier tungsten atom. The sulfur atom is seen to contribute to the other two conduction-band valleys between the Γ-K and M-Γ points. For the WS_2
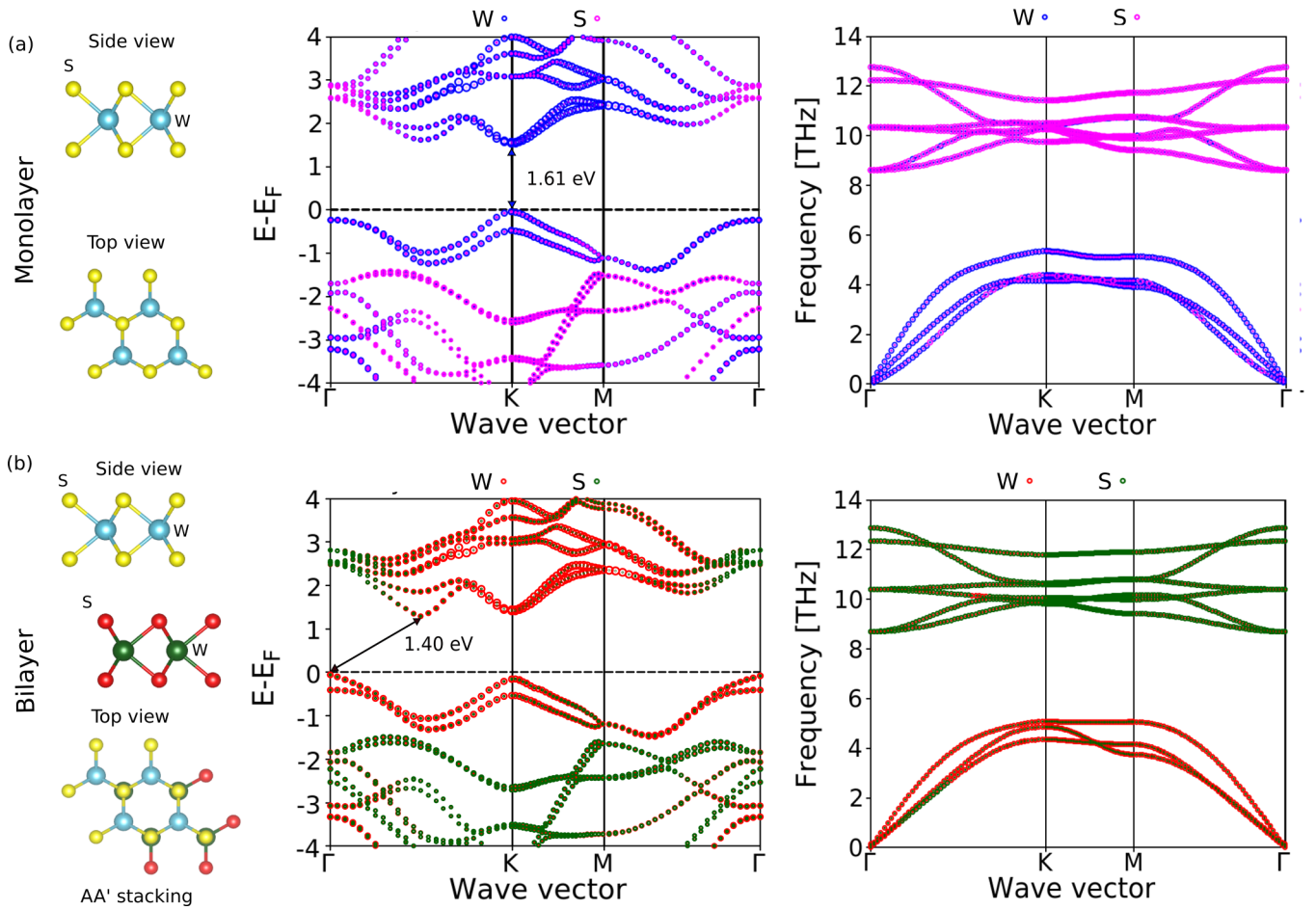
FIG. 1. Top and side view of crystal structure, atom-projected electronic band structure by including SOC (second figure in each row) and phonon band structure (third figure in each row) of (a) monolayer and (b) bilayer WS$_2$. The bilayer WS$_2$ is shown in its AA' stacking type.

bilayer, the CBM is located at the midpoint between Γ and K, while the VBM is located at the Γ point. The bilayer WS$_2$ has a band gap of 1.40 eV, which is less than its monolayer due to the strong quantum confinement effect exhibited in the monolayer. The CBM and VBM are dominated by the contribution from the tungsten atom in bilayer WS$_2$. The bilayer has overlapping conduction valleys. Both of these materials have multiple conduction-band valleys within a narrow energy range near the Fermi level, prompting intervalley transitions in these materials. The lowest conduction band of monolayer WS$_2$ has three valleys, while bilayer WS$_2$ has six valleys.

The dynamic stability of both of these layers is established from non-negative phonon-dispersion curves shown in the third column of Fig. 1. As seen from the figure, in the case of the monolayer, lower-frequency acoustic modes are dominated by tungsten atoms, but in the bilayer, both tungsten and sulfur atoms contribute to the low-frequency TA acoustic modes. The contribution of atoms reverses for higher-frequency modes. The sulfur atoms dominate the optical modes in monolayer WS$_2$. In bilayer WS$_2$, the first three optical modes lie very close to acoustic modes with frequencies 0.093, 0.093, and 0.163 THz at the Γ point (see Fig. S1 in the Supplemental Material [45]). The remaining optical modes have frequencies greater than 8 THz. Tungsten atoms dominate the first three optical modes, but

sulfur atoms dominate the high-frequency optical modes. WS$_2$ monolayer shows a more quadratic nature of acoustic modes than bilayer, implying greater anharmonicity. The steepness of acoustic bands along the Γ-K direction in bilayer WS$_2$ as compared to monolayer WS$_2$ suggests that the group velocity of phonons of bilayer WS$_2$ will be higher than monolayer WS$_2$. Both anharmonicity and group velocity are parameters that play an essential role in phonon transport.

The relaxation time of electrons forms an integral part of the transport distribution function, which is used to calculate the electrical transport coefficients. Figure 2 shows the variation of relaxation time with energy as well as temperature on including different scattering mechanisms for monolayer and bilayer WS$_2$. As calculated from the model [Eq. (5)], the electron–acoustic-phonon relaxation time ($\tau_{e\text{-ph}_{ac}}$) is comparable for both monolayer and bilayer WS$_2$ [see Figs. 2(a) and 2(c)] due to similar values of the speed of sound and acoustic deformation potential. The scattering rates calculated by PERTURBO [22] also exhibit the same nature. This relaxation time decreases as we move away from the band edges, and it follows the pattern of the density of states. The elevated electron–acoustic-phonon relaxation times in the order of picoseconds for both systems indicate that other scattering mechanisms are active in these materials. The relaxation time due to the interaction of optical phonons with electrons is
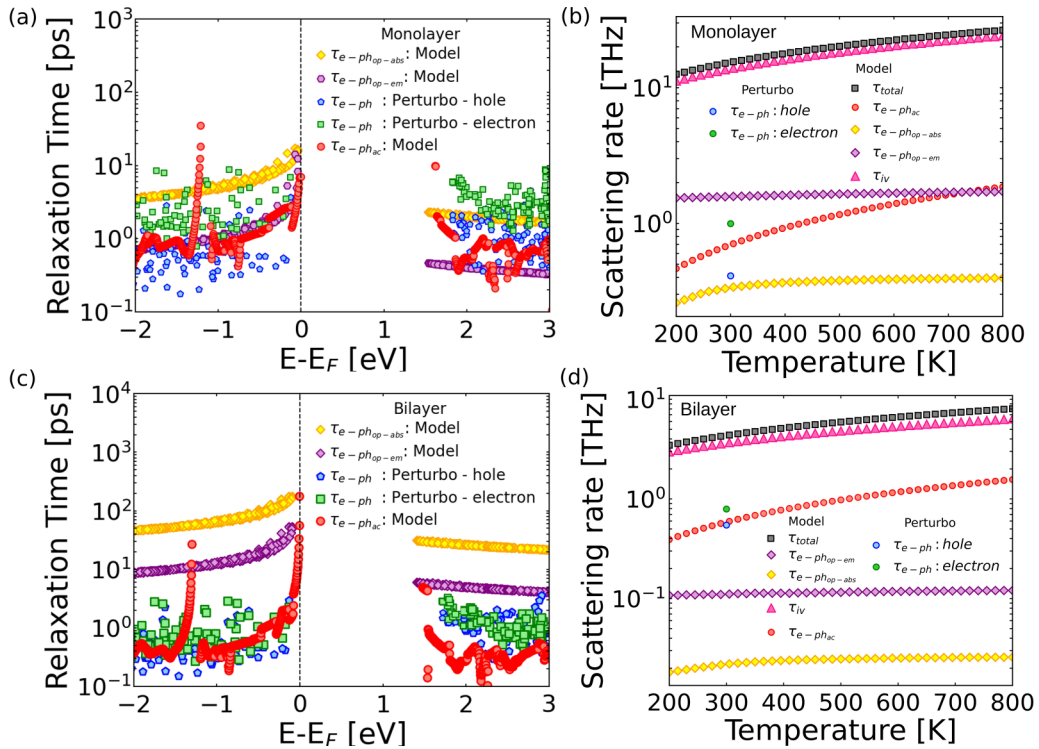
FIG. 2. Variation of relaxation time with energy $(E-E_F)$ due to electron–acoustic-phonon scattering ($\tau_{e\text{-ph}_{ac}}$, red) and electron–optical-phonon scattering ($\tau_{e\text{-ph}_{op\text{-}abs}}$, yellow diamond; $\tau_{e\text{-ph}_{op\text{-}em}}$, purple diamond) calculated using the model and full solution to the e-ph scattering matrix using PERTURBO (blue circles for electrons and green circles for holes) for (a) monolayer and (c) bilayer WS$_2$, respectively, at 300 K. Variation of the above-mentioned scattering rates along with intervalley scattering (τ_{iv}, pink triangle) and total scattering (τ_{total}, black square) with temperature for (b) monolayer and (d) bilayer WS$_2$.

also considered. The electrons get scattered by optical-phonon modes when their energy becomes comparable. From the temperature-dependent scattering rate plot for the monolayer [see Fig. 2(b)], it is seen that at temperatures between 200 and 500 K, the electron–acoustic-phonon scattering rate and electron–optical-phonon absorption scattering rates are in the same range, while above 500 K the scattering rates due to the optical-phonon emission process is closer to the electron–acoustic-phonon scattering. For the case of bilayer WS$_2$, the contribution from the electron–optical-phonon scattering process is less as compared to the contribution due to acoustic phonons [see Figs. 2(c) and 2(d)]. This is due to the wide range of optical-phonon frequencies ranging from 0.5 to 14 THz [Eq. (6)]. Monolayer and bilayer WS$_2$, within a small energy range near the Fermi level, have multiple valleys. The electrons and holes can scatter from one valley to another, causing intervalley scattering. This scattering mechanism is generally overlooked but must be considered, as it can significantly influence electrical transport properties. Therefore, for both monolayer and bilayer WS$_2$, this scattering is incorporated [see Fig. 2(b)]. For the case of monolayer WS$_2$, strong intervalley scattering is seen. For the case of bilayer WS$_2$, the intervalley scattering is less as compared to monolayer, which is due to more aligned valleys and lower-frequency optical-phonon modes taking part in the carriers' transition from the initial to the final state. The total scattering rate for both materials is dominated by intervalley scattering. At 300 K, the scattering rate increases by ∼21 times for monolayer and ∼7

times for bilayer WS$_2$ on considering intervalley transitions. This will greatly influence the electrical transport properties.

The electrical transport properties of monolayer and bilayer WS$_2$ within the temperature range 200–800 K are calculated at a carrier concentration of 3.3×10^{13} cm^{-2} where the maximum power factor is attained. The effect of including all scattering mechanisms on electrical conductivity (σ) and the Seebeck coefficient (S) is plotted in Fig. 3 for both monolayer and bilayer WS$_2$. The first column of the figure represents transport properties calculated considering only electron–acoustic-phonon scattering. Though this relaxation time of carriers for both materials is comparable, the electrical conductivity of monolayer WS$_2$ is higher. This is because the group velocity of electrons is more in monolayer WS$_2$, which affects the transport distribution function and hence the electrical transport properties. The Seebeck coefficient is also high in monolayer WS$_2$ due to the increase in the band gap and the density of states near the Fermi level (see Fig. S2 in the supplemental material [45]). The second column of Fig. 3 shows the change in electrical conductivity and Seebeck coefficient on including electron–optical-phonon scattering. As scattering rates due to both acoustic and optical phonons in monolayer WS$_2$ are in close proximity to each other, as shown in Fig. 2, they strongly affect the electrical conductivity [see Fig. 3(b)] and reduce it by 73%. The Seebeck coefficient, however, increases only slightly by 5%. For the case of the bilayer [see Fig. 3(e)], the electrical conductivity reduces by only 18%, and hardly any change is observed for Seebeck
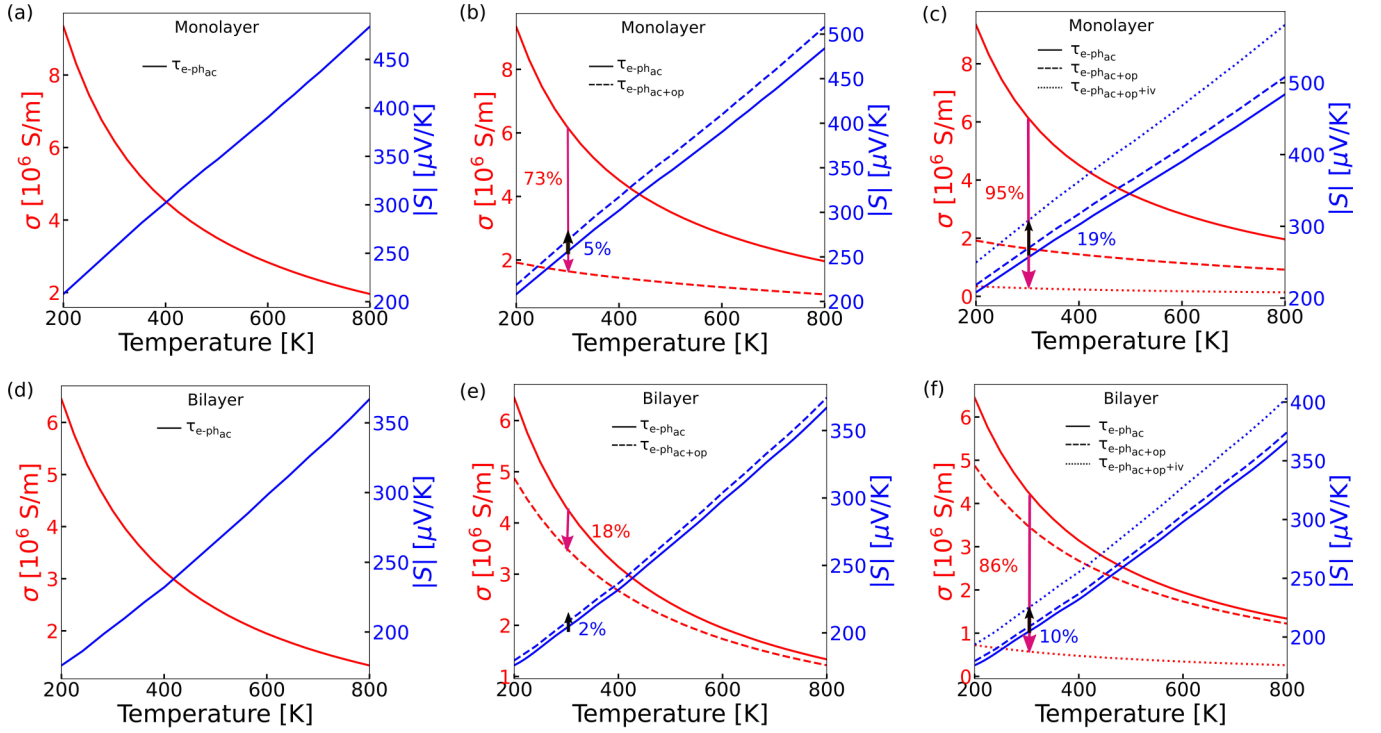
FIG. 3. Variation of electrical conductivity (σ, red) and Seebeck coefficient (S, blue) for monolayer (a)–(c) and bilayer (d)–(f) WS$_2$ with the temperature at a carrier concentration of 3.3×10^{-13} cm^{-2} on considering the effect of electron–acoustic-phonon scattering (first figure in each row), electron–acoustic-phonon and electron–optical-phonon scattering (second figure in each row), and finally including intervalley scattering (third figure in each row). The arrows represent the percentage change in electrical conductivity (black) and Seebeck coefficient (magenta) when electron–optical-phonon scattering and intervalley scattering are included.

coefficient values. This is because the scattering of electrons due to optical phonons is not active in the bilayer. Intervalley scattering has the strongest effect on transport properties for both materials, which can be attributed to the multiple valleys in close proximity to the Fermi level, allowing electron transitions. The electrical conductivity reduces by 95% and 86% for monolayer and bilayer, respectively. The reduction in the bilayer is less because of lower scattering due to more aligned valleys. In contrast to electrical conductivity values, intervalley scattering increases the Seebeck coefficient by 19% and 10% for monolayer and bilayer, respectively.

Combining the electrical conductivity and Seebeck coefficient values, the power factor for monolayer and bilayer WS$_2$ is calculated, as shown in Figs. 4(a) and 4(b). For monolayer WS$_2$, the power factor increases with temperature. The intervalley scattering potentially reduces the power factor by 93%. For the case of bilayer WS$_2$, when the impact of both acoustic and optical phonon interactions with electrons is seen, the power factor decreases until 400 K and then increases. But when intervalley scattering is included, the power factor increases with temperature. The similar percentage reductions of electrical conductivity and power factor on including intervalley scattering show that the power factor is mainly influenced by electrical conductivity even though it has a squared dependence on the Seebeck coefficient. A maximum power factor of $\sim$48 mW m^{-1} K^{-2} is obtained for monolayer while $\sim$43 mW m^{-1} K^{-2} is attained for bilayer WS$_2$ at 800 K. These values are very close to each other. Thus, to better

compare the thermoelectric efficiency of both materials, evaluation of thermal transport properties is important.

Electronic thermal conductivity (κ_e), as shown in Fig. 5(a), is also calculated for both monolayer and bilayer WS$_2$ considering all scattering mechanisms. Inclusion of intervalley scattering leads to negligible values of 0.95 W m^{-1} K^{-1} for monolayer WS$_2$. Figure 5(b) depicts the lattice thermal conductivity (κ_l) for temperatures ranging from 200 to 800 K. The κ_l values calculated using the τ_U model for monolayer WS$_2$ show a remarkable agreement of over 98% with the values calculated using the RTA approach, as implemented in ALMABTE. This agreement is highlighted in Fig. S3 of the supplemental material [45], where κ_l values for five other chalcogenides have been computed using both methods, and they also show good agreement with each other [12,46–48]. In addition to the RTA approach, the κ_l values are also calculated using the full solution to BTE, as implemented in the ALMABTE software, and they are found to agree well with previously reported SHENGBTE values [15,49,50]. However, the κ_l values calculated using the full solution to BTE are approximately 3.5 times higher, while the κ_l values calculated using the RTA approach are approximately two times higher than the experimental values reported by Peimyoo *et al.* [16]. This disagreement with the experimental data prompted us to investigate other scattering mechanisms that could be influencing the lattice thermal conductivity of these layers.

As experimentally the formation of WS$_2$ monolayer or bilayer can lead to the presence of sulfur vacancies, we include
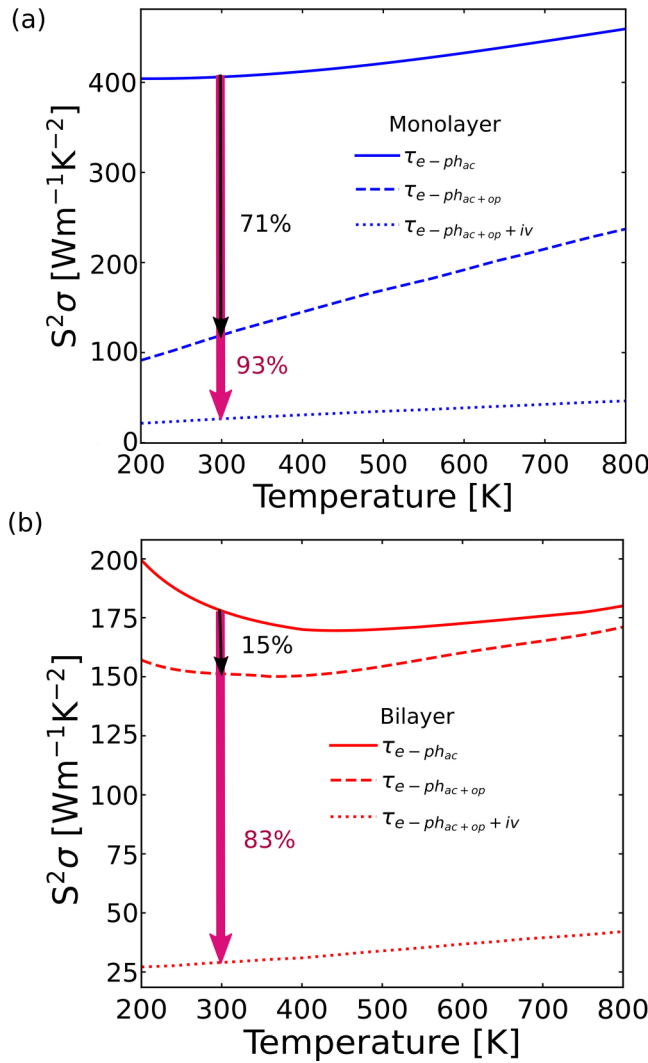
FIG. 4. Variation of power factor with temperature for (a) monolayer and (b) bilayer WS$_2$. The solid line represents values calculated using electron–acoustic-phonon relaxation time. The dashed lines represent values calculated using both electron–acoustic-phonon and electron–optical-phonon relaxation time. The dotted lines represent values calculated using intervalley scattering as well. The arrows represent the percentage change in power factor values when electron–optical-phonon (black) and intervalley scattering is included (magenta).

FIG. 5. (a) Variation of electronic thermal conductivity with temperature for monolayer and bilayer WS$_2$ considering all scattering mechanisms. (b) Variation of lattice thermal conductivity (κ_l) with temperature for WS$_2$ monolayer and bilayer by employing all scattering mechanisms. The solid blue line with a triangle represents κ_l values of monolayer WS$_2$ calculated using the full solution to BTE, while the solid blue line with a circle represents κ_l values of monolayer WS$_2$ calculated using the RTA approach using ALMABTE. The experimental data available for these two layers at 300 K are plotted as circle, bilayer; and square, monolayer [16].

phonon scattering due to the presence of these vacancies for a relative vacancy concentration of $c = 0.03$ corresponding to the experimental W:S ratio [38]. A significant reduction in the lattice thermal conductivity values is seen on including this scattering [see Fig. 5(b)]. We conducted additional calculations to investigate the impact of an increase in sulfur vacancies on the lattice thermal conductivity of monolayer WS$_2$ at room temperature. The results shown in Fig. S5 of the supplemental material [45] reveal that at 300 K, an increase in defect concentration leads to a reduction in the lattice thermal conductivity. Consequently, a sample consisting of numerous sulfur vacancies can achieve an extremely low lattice thermal conductivity value. In these materials, in the presence of a significant number of vacancies ($c > 0.01$; see Fig. S5 in
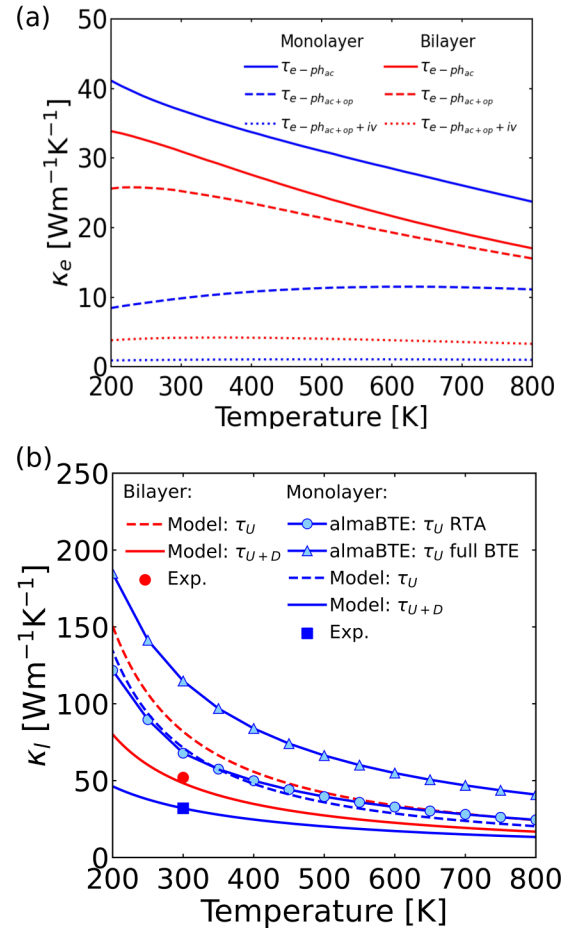
the supplemental material [45]), defect scattering is seen to be the dominant phonon scattering mechanism. At $c = 0.03$, the relaxation time due to defect scattering dominates at all temperatures (see Fig. S4 in the supplemental material [45]). Hence, as seen from the plot, the inclusion of this scattering mechanism leads to ~50% reduction in κ_l values. The total thermal conductivity is in ~99% agreement with the experimental values [16]. Therefore, for the TMDs with a significant number of vacancies, defect scattering is the dominant scattering mechanism.

Next, using the transport coefficients, the figure of merit (ZT) (see Fig. 6) is calculated as a function of temperature. Deceptive values of $ZT \sim 5$ for bilayer and $ZT \sim 10$ for monolayer at 800 K can be obtained if only electron–acoustic-phonon scattering is considered. After including electron–optical-phonon scattering, ZT reduces by 20% for monolayer WS$_2$, while it remains almost the same for bi-
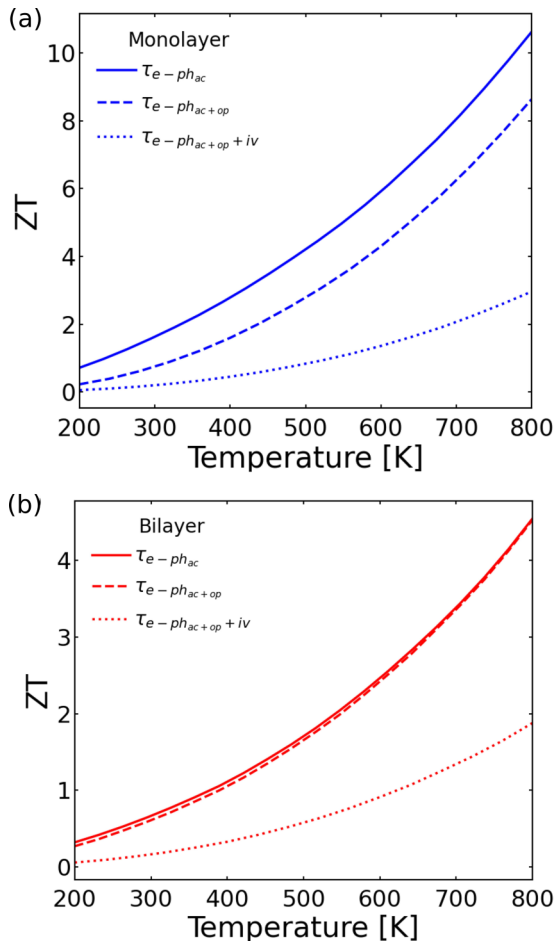
FIG. 6. Variation of ZT with temperature for (a) monolayer (blue) and (b) bilayer (red) WS$_2$. The solid line represents values calculated using electron–acoustic-phonon relaxation time. The dashed lines represent values calculated using intravalley electron–acoustic-phonon and electron–optical-phonon relaxation time. The dotted lines represent values calculated using the intervalley scattering mechanism as well.

layer WS$_2$. Finally, upon including the intervalley scattering process for electrical transport properties and defect-phonon scattering for thermal transport properties calculation, $ZT \sim 3$ and $ZT \sim 2$ are achieved for monolayer and bilayer WS$_2$, respectively, at 800 K. After inclusion of all scattering mechanisms, ZT of the monolayer is still about seven times higher than that of its bulk counterpart [6]. Even though the power

factor is almost the same for both monolayer and bilayer WS$_2$, the figure of merit is more for monolayer than bilayer because of lower lattice thermal conductivity. For both materials, $ZT > 1$ can be achieved at temperatures greater than 500 K. As these materials are multivalley semiconductors, the room-temperature thermoelectric properties can be further enhanced by band alignment, which can enable a higher Seebeck coefficient, keeping the electrical conductivity the same, thereby giving rise to higher power factor values. This can be controlled via doping and alloying [51].

IV. CONCLUSION

In conclusion, we calculated the thermoelectric transport properties of monolayer and bilayer TMD WS$_2$ by including intravalley and intervalley electron-phonon scattering. Our study points to the importance of intervalley scattering in electrical transport in these materials due to the presence of three valleys in the conduction band of monolayer and six valleys in the conduction band of bilayer WS$_2$ in the vicinity of the Fermi level. After including intervalley scattering, electrical conductivity reduced from 6.13×10^6 to 2.74×10^5 S/m for monolayer WS$_2$, while it reduced from 4.22×10^6 to 5.78×10^5 S/m for bilayer WS$_2$ at 300 K. This led to significant deterioration of the power factor by 93% in monolayer and 83% in bilayer WS$_2$. In the case of thermal transport properties calculation, the umklapp scattering rate or phonon-phonon scattering rate overestimates the lattice thermal conductivity values. Defect scattering plays a crucial role in reducing lattice thermal conductivity in monolayer and bilayer WS$_2$ when the relative sulfur vacancy concentration exceeds 0.01. Incorporating the influence of defect scattering on thermal transport results in a remarkable 99% agreement with experimental values for both layers. The combined effect of high power factor and low lattice thermal conductivity in monolayer and bilayer WS$_2$ leads to high values of $ZT \sim 3$ for monolayer and $ZT \sim 2$ for bilayer at 800 K. Our analysis provides a deeper understanding of the role of different scattering mechanisms that can tune the transport properties of monolayer and bilayer WS$_2$. Similar studies can also be applied to other 2D TMDs showing the same band characteristics.

[1] Q. H. Wang, K. Kalantar-Zadeh, A. Kis, J. N. Coleman, and M. S. Strano, Nat. Nanotechnol. **7**, 699 (2012).

[2] H. Shi, R. Yan, S. Bertolazzi, J. Brivio, B. Gao, A. Kis, D. Jena, H. G. Xing, and L. Huang, ACS Nano **7**, 1072 (2013).

[3] W. Li, J. Carrete, and N. Mingo, Appl. Phys. Lett. **103**, 253103 (2013).

[4] Y. Cai, G. Zhang, and Y.-W. Zhang, J. Am. Chem. Soc. **136**, 6269 (2014).

[5] M. Buscema, M. Barkelid, V. Zwiller, H. S. J. van der Zant, G. A. Steele, and A. Castellanos-Gomez, Nano Lett. **13**, 358 (2013).

[6] A. N. Gandi and U. Schwingenschlögl, Chem. Mater. **26**, 6628 (2014).

[7] D. Wickramaratne, F. Zahid, and R. K. Lake, J. Chem. Phys. **140**, 124710 (2014).

[8] J. K. Gustafson, P. D. Cunningham, K. M. McCreary, B. T. Jonker, and L. M. Hayden, J. Phys. Chem. C **123**, 30676 (2019).

[9] W. Huang, X. Luo, C. K. Gan, S. Y. Quek, and G. Liang, Phys. Chem. Chem. Phys. **16**, 10866 (2014).

[10] T. Li and G. Galli, J. Phys. Chem. C **111**, 16192 (2007).

[11] D. Xiao, G.-B. Liu, W. Feng, X. Xu, and W. Yao, Phys. Rev. Lett. **108**, 196802 (2012).

[12] R. Gupta, B. Dongre, J. Carrete, and C. Bera, J. Appl. Phys. **130**, 054301 (2021).

[13] R. Gupta, N. Kumar, P. Kaur, and C.Bera, Phys. Chem. Chem. Phys. **22**, 18989 (2020).

[14] V. Askarpour and J. Maasen, Phys. Rev. B **107**, 045203 (2023).

[15] M. Zulfiqar, Y. Zhao, G. Li, Z. Li, and J. Ni, Sci. Rep. **9**, 4571 (2019).

[16] N. Peimyoo, J. Shang, W. Yang, Y. Wang, C. Cong, and T. Yu, Nano Res. **8**, 1210 (2015).

[17] C. Liu, M. Yao, J. Yang, J. Xi, and X. Ke, Mater. Today Phys. **15**, 100277 (2020).

[18] P. E. Blöchl, Phys. Rev. B **50**, 17953 (1994).

[19] G. Kresse and D. Joubert, Phys. Rev. B **59**, 1758 (1999).

[20] J. P. Perdew, K. Burke, and M. Ernzerhof, Phys. Rev. Lett. **77**, 3865 (1996).

[21] G. K. H. Madsen, J. Carrete, and M. J. Verstraete, Comput. Phys. Commun. **231**, 140 (2018).

[22] J.-J. Zhou, J. Park, I.-T. Lu, I. Maliyov, X. Tong, and M. Bernardi, Comput. Phys. Commun. **264**, 107970 (2021).

[23] A. Togo, F. Oba, and I. Tanaka, Phys. Rev. B **78**, 134106 (2008).

[24] J. Bardeen and W. Shockley, Phys. Rev. **80**, 72 (1950).

[25] A. Rawat, N. Jena, D. Dimple, and A. D. Sarkar, J. Mater. Chem. A **6**, 8693 (2018).

[26] W. Zhang, Z. Huang, W. Zhang, and Y. Li, Nano Res. **7**, 1731 (2014).

[27] Z. Jin, X. Li, J. T. Mullen, and K. W. Kim, Phys. Rev. B **90**, 045422 (2014).

[28] P. Giannozzi, S. Baroni, N. Bonini, M. Calandra, R. Car, C. Cavazzoni, D. Ceresoli, G. L. Chiarotti, M. Cococcioni, I. Dabo, A. D. Corso, S. de Gironcoli, S. Fabris, G. Fratesi, R. Gebauer, U. Gerstmann, C. Gougoussis, A. Kokalj, M. Lazzeri, L. Martin-Samos *et al.*, J. Phys.: Condens. Matter **21**, 395502 (2009).

[29] N. Marzari and D. Vanderbilt, Phys. Rev. B **56**, 12847 (1997).

[30] I. Souza, N. Marzari, and D. Vanderbilt, Phys. Rev. B **65**, 035109 (2001).

[31] W. A. Harrison, Phys. Rev. **104**, 1281 (1956).

[32] E. M. Conwell, *High Field Transport in Semiconductors*, Solid State Physics/Supplement 9 (Academic Press, New York, 1967).

[33] A. Togo and I. Tanaka, Scr. Mater. **108**, 1 (2015).

[34] L. Bjerg, B. B. Iversen, and G. K. H. Madsen, Phys. Rev. B **89**, 024304 (2014).

[35] R. Gupta, B. Kaur, J. Carrete, and C. Bera, J. Appl. Phys. **126**, 225105 (2019).

[36] G. A. Slack, Solid State Phys. **34**, 1 (1979).

[37] G. K. H. Madsen, A. Katre, and C. Bera, Phys. Status Solidi A **213**, 802 (2016).

[38] C. Cong, J. Shang, X. Wu, B. Cao, N. Peimyoo, C. Qiu, L. Sun, and T. Yu, Adv. Opt. Mater. **2**, 131 (2013).

[39] P. G. Klemens, Phys. B: Condens. Matter **263-264**, 102 (1999).

[40] J. Carrete, B. Vermeersch, A. Katre, A. van Roekeghem, T. Wang, G. K. Madsen, and N. Mingo, Comput. Phys. Commun. **220**, 351 (2017).

[41] J. Carrete, W. Li, L. Lindsay, D. A. Broido, L. J. Gallego, and N. Mingo, Mater. Res. Lett. **4**, 204 (2016).

[42] W. Li, J. Carrete, N. A. Katcho, and N. Mingo, Comput. Phys. Commun. **185**, 1747 (2014).

[43] C. Yelgel, Ö. C. Yelgel, and O. Gülseren, J. Appl. Phys. **122**, 065303 (2017).

[44] W. Li, T. Wang, X. Dai, X. Wang, C. Zhai, Y. Ma, and S. Chang, Solid State Commun. **225**, 32 (2016).

[45] See Supplemental Material at http://link.aps.org/supplemental/10.1103/PhysRevB.108.115406 for more information on electronic density of states and phonon transport properties of monolayer and bilayer WS$_2$.

[46] R. Gupta, S. Kakkar, B. Dongre, J. Carrete, and C. Bera, ACS Appl. Energy Mater. **6**, 3944 (2023).

[47] R. Gupta, B. Dongre, C. Bera, and J. Carrete, J. Phys. Chem. C **124**, 17476 (2020).

[48] B. Kaur, R. Gupta, S. Dhiman, K. Kaur, and C. Bera, Phys. B: Condens. Matter **661**, 414898 (2023).

[49] Z. Zhang, Y. Xie, Y. Ouyang, and Y. Chen, Int. J. Heat Mass Transf. **108**, 417 (2017).

[50] D. Han, H. Sun, W. Ding, Y. Chen, X. Wang, and L. Cheng, Physica E **124**, 114312 (2020).

[51] P. Kaur, G. K. H. Madsen, and C. Bera, MRS Commun. **9**, 370 (2019).